Complex Data Analysis in High-Resolution SSFP fMRI

Jongho Lee,[1][*] Morteza Shahram,[2] Armin Schwartzman,[3,4] and John M. Pauly[1]

In transition-band steady-state free precession (SSFP) functional MRI (fMRI), functional contrast originates from a bulk frequency shift induced by a deoxygenated hemoglobin concentration change in the activated brain regions. This frequency shift causes a magnitude and/or phase-signal change depending on the off-resonance distribution of a voxel in the balanced-SSFP (bSSFP) profile. However, in early low-resolution studies, only the magnitude signal activations were shown. In this paper the task-correlated phase-signal change is presented in a high-resolution ($1 \times 1 \times 1$ mm^3) study. To include this phase activation in a functional analysis, a new complex domain data analysis method is proposed. The results show statistically significant phase-signal changes in a large number of voxels comparable to that of the magnitude-activated voxels. The complex-data analysis method successfully includes these phase activations in the activation map and thus provides wider coverage compared to magnitude-data analysis results. **Magn Reson Med 57:905–917, 2007. © 2007 Wiley-Liss, Inc.**

Key words: complex; multivariate; SSFP; phase activation; BOSS

Since its first inception in the early 1990s, blood oxygen level-dependent (BOLD) functional MRI (fMRI) has had a tremendous impact on human brain research. Most studies performed a functional data analysis using the magnitude data of the time-series images while ignoring phase-signal changes. Recently a few high-resolution studies explored the phase information and revealed that the task-correlated phase-signal change can provide additional information regarding brain activation (1,2). Investigators found that a large draining vein induced phase-signal changes in addition to magnitude-signal changes by creating a relatively uniform frequency shift within a voxel. This information was utilized to determine the oxygen saturation change in veins (1) and to suppress BOLD signals from large vessels (2). However, in transition-band SSFP, or blood oxygenation sensitive steady state (BOSS) fMRI, a recently developed functional imaging method that provides greater signal-to-noise ratio (SNR) efficiency with less imaging distortion (3–6), the origin of the phase-signal change differs from that in conventional gradient-recalled echo (GRE) fMRI (5). Moreover, this task-correlated phase-

signal change was always expected, since a sharp phase transition near the on-resonance frequency (also at every multiple of 1/TR) is considered to be a primary source of the functional contrast in transition-band SSFP fMRI. However, early low-resolution studies measured functional activations from the magnitude signals (5). This has raised questions regarding the existence of the phase activation and the contribution of the SSFP phase profile to the functional contrast. In this article we present the results of a 3D high-resolution (1 mm^3) functional study to show the presence and characteristics of task-correlated phase-signal changes in transition-band SSFP fMRI. Simulation results are also included to further elucidate the sensitivity and characteristics of the phase-signal changes.

If functional contrast exists in both magnitude and phase signals, and if both signals provide spatially localized information, an analysis based only on magnitude cannot fully exploit the data. Some voxels that contain phase activation without magnitude activation will not be detected, and some voxels that contain both activations will show less activation in the magnitude-only analysis. Therefore, to acquire more reliable results, a complex domain data analysis method that encompasses both magnitude- and phase-signal activations is necessary. Recently several complex-data analysis methods (7–15), most of which are based on a generalized likelihood ratio test (GLRT) (13), have been proposed. Here we propose a new method that combines a Hotelling's T^2-test (which can be derived from GLRT) (16) with a generalized linear model (GLM) (17) to calculate the statistical significance of the activation from complex data. This method is computationally efficient compared to the previously proposed methods, and generates full activation maps that include both magnitude and phase activations.

THEORY

Functional Contrast of Transition-Band SSFP fMRI

Unlike the contrast mechanism of $T_2{}^*$ dephasing in conventional GRE fMRI, transition-band SSFP fMRI is based on a bulk frequency shift induced by a fractional oxygen saturation change of hemoglobin (4,5). This frequency shift is a function of vessel orientations, the fractional oxygen saturation of hemoglobin, and the magnetic field strength. If a cylindrical vessel tilted by θ degree with respect to the main field is assumed, the intra- (Δf_{iv}) and extravascular (Δf_{ev}) frequency shifts are given by (18,19):

$$\Delta f_{iv} = \gamma Hct\Delta\chi(1 - Y)B_0(\cos^2\theta - 1/3) \qquad [1]$$

$$\Delta f_{ev} = \gamma Hct\Delta\chi(1 - Y)B_0(R/|\mathbf{r}|)^2\sin^2\theta\cos(2 \angle \mathbf{r}), \quad [2]$$

where γ is the gyromagnetic ratio (2.678×10^8 rad T^{-1} s^{-1}), Hct is a fractional hematocrit in blood (0.4), $\Delta\chi$ is the susceptibility difference between fully oxygenated and fully deoxygenated red blood cells (0.27 ppm from Ref.

[1]Magnetic Resonance Systems Research Laboratory, Department of Electrical Engineering, Stanford University, Stanford, California, USA.

[2]Department of Statistics, Stanford University, Stanford, California, USA.

[3]Department of Biostatistics, Harvard School of Public Health and Dana-Farber Cancer Institute, Boston, Massachusetts, USA.

[4]Department of Biostatistics, and Computational Biology, Dana-Farber Cancer Institute, Boston, Massachusetts, USA.

*Correspondence to: Jongho Lee, Room 208, Packard Electrical Engineering Bldg., Stanford University, Stanford, CA 94305-9510. E-mail: jonghoyi@mrsrl.stanford.edu

Magnitude profile

a

Phase profile

b

c
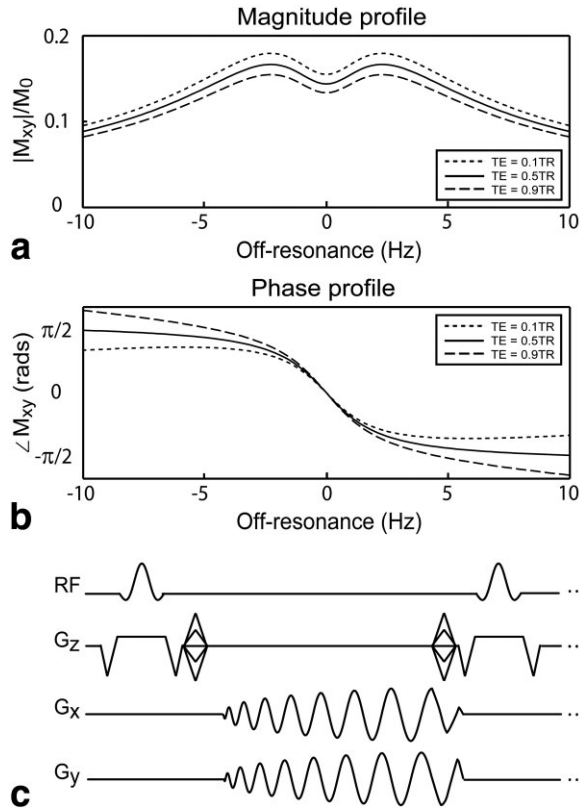
FIG. 1. Small-flip-angle bSSFP (**a**) magnitude and (**b**) phase profiles at three different TEs (TE = 0.1TR, 0.5TR, and 0.9TR). The frequency sensitivity of these profiles provides the functional contrasts of transition-band SSFP fMRI. **c:** 3D interleaved stack-of-spirals sequence for the functional scan.

20), Y is the fractional oxygen saturation of hemoglobin, R is the radius of the vessel, and $\mathbf{r}$ is a vector from the center axis of the vessel on an orthogonal plane of the vessel.

The magnitude and phase signals of a voxel are determined by the intra- and extravascular frequency shifts, the fractional volume of the vessels, and the off-resonance frequency distribution. If a voxel contains n veins whose volumes are small (and the veins are distant from each other), and the off-resonance frequency distribution of the voxel is assumed to be uniform, then the magnetization of the voxel (M) becomes

$$\mathrm{M} = (1 - \alpha)\mathrm{P}(f_{off}) + \sum_{i=0}^{n}\left\{\int_{\alpha_i}\mathrm{P}(f_{off} + \Delta f_i)d\alpha_i\right\}, \qquad [3]$$

where α is the total volume of all veins (including extravascular spaces), f_{off} is the off-resonance frequency of the voxel, α_i is the volume of the ith vein (including the extravascular space), Δf_i is the fractional frequency shift from the off-resonance frequency induced by the ith vein in the $d\alpha_i$ space, and P is the magnetization profile of balanced SSFP (bSSFP; Fig. 1a and b).

If a vessel is located near the resonance frequency, the sharp phase transition will create a large phase-signal change in accordance with the bulk frequency shift. As a

result, a task-correlated phase-signal change is expected. Based on the orientation of the vessel, the intravascular frequency shift can cause either a positive ($|\theta| < 0.96$ or $2.19 < |\theta| < 3.14$ radian) or a negative ($0.96 < |\theta| < 2.19$ radian) phase change, resulting in two different phase correlations. The extravascular frequency shift can also contribute to the net phase accrual due to the nonlinear phase profile. However, if a voxel is large and only a fractional volume of the vessels shows oxygen concentration changes, and the vessels are randomly oriented, then the task-correlated phase-signal change will be decreased due to partial-volume effects and incoherent phase accruals. As a result, in low-resolution studies the phase-signal change is difficult to observe, even in the phase transition band.

Outside of the phase transition band, the bulk frequency shift (Δf) modulates the magnitude signal from the magnitude profile with little or no phase-signal change. Both a positive and a negative magnitude change can be detected based on the off-resonance frequency and vessel orientation. For instance, if the off-resonance frequency shift is positive and a vessel is parallel to the field, the voxel will show a positive correlation with the given stimulus, whereas a vein tilted by a $\pi/2$ radian will show a negative correlation.

Hotelling's T²-Test

In conventional fMRI analysis, where there is only one variate (magnitude data), a Student's t-test can be used to determine whether the null hypothesis is rejected (i.e., the voxel shows activation) or is not rejected (i.e., the voxel shows no activation) for a given threshold. However, in the complex data analysis, the number of variates becomes two (i.e., real and imaginary or magnitude and phase); hence, one must generalize the Student's t-test to a bivariate test to evaluate the null hypothesis in the complex domain. This generalization can be achieved using a Hotelling's T²-test (16) that compares the sample mean vector with the expected mean vector, and performs the null hypothesis test on a multivariate domain as described below.

Similarly to the Student's t-test statistic $t = (\bar{x} - \mu)/(\hat{\sigma}/\sqrt{n})$, (where n is the number of samples, $\bar{x}$ is the sample mean, μ is the hypothetical population mean, and $\hat{\sigma}$ is the sample standard deviation (SD)), the Hotelling's T²-test is defined as

$$\mathrm{T}^2 = (\bar{\mathbf{x}} - \boldsymbol{\mu})^{\mathrm{T}}(\hat{\mathbf{S}}/n)^{-1}(\bar{\mathbf{x}} - \boldsymbol{\mu}), \qquad [4]$$

where n is the number of samples, $\bar{\mathbf{x}}$ is the sample mean vector, $\boldsymbol{\mu}$ is the hypothetical population mean vector, and $\hat{\mathbf{S}}$ is the sample covariance matrix (an unbiased estimator). When the sample has two variates (for example, real and imaginary), $\bar{\mathbf{x}}$ and $\boldsymbol{\mu}$ become 2×1 vectors, whereas $\hat{\mathbf{S}}$ becomes a 2×2 matrix.

If all of the variates (in this case, both the real and imaginary parts of the data) are distributed by the Gaussian distribution, the T² statistic will follow an F-distribution with m and $n\text{-}m$ degrees of freedom (where m is the number of variates in the sample (i.e., $m = 2$ in the complex data) and n is the number of samples). This T² statistic can

be derived from a likelihood ratio test (a full derivation can be found in Ref. 16). For a given significance level α, the null hypothesis is rejected when

$$T^2 > \left[\frac{(n-1)m}{n-m}\right]F_{m,n-m}(\alpha). \quad [5]$$

A *P*-value can be obtained from the cumulative distribution function (CDF) of $F_{m,n-m}$ evaluated at $T^2(n-m)/[(n-1)m]$.

$$p = 1 - \text{CDF of } F_{m,n-m}\left[T^2\frac{n-m}{(n-1)m}\right]. \quad [6]$$

Complex Data Analysis Method

To incorporate the hemodynamic response function into this T^2-test, a GLM (17) is utilized to estimate the mean vectors of the activation and baseline states, as well as the covariance matrix. The complex time-series data are decomposed into real and imaginary axes. To find the mean vector of each state, one structures the design matrix ($\mathbf{X}$) of the GLM by a constant vector ($\mathbf{1} = [1 \ 1 \ \ldots . \ 1]^T$, a real $n \times 1$ vector) and a reference waveform vector ($\mathbf{h}$, a real $n \times 1$ vector, the convolution of a stimulus pattern and a hemodynamic response function). Equation [7] shows this modeling:

$$\mathbf{y_r} = \mathbf{X}\boldsymbol{\beta_r} + \boldsymbol{\varepsilon_r} = [\mathbf{l} \quad \mathbf{h}][\beta_{r1} \quad \beta_{r2}]^T + \boldsymbol{\varepsilon_r} \quad [7]$$

$$\mathbf{y_i} = \mathbf{X}\boldsymbol{\beta_i} + \boldsymbol{\varepsilon_i} = [\mathbf{l} \quad \mathbf{h}][\beta_{i1} \quad \beta_{i2}]^T + \boldsymbol{\varepsilon_i},$$

where $\mathbf{y} = \mathbf{y_r} + i\mathbf{y_i}$ (a complex $n \times 1$ vector) is the time-series data of one voxel, $\boldsymbol{\beta_r}$ and $\boldsymbol{\beta_i}$ (a real 2×1 vector each) are the parameters of GLM, and $\boldsymbol{\varepsilon_r}$ and $\boldsymbol{\varepsilon_i}$ are residual errors (a real $n \times 1$ vector each). One can easily incorporate other terms, such as a linear drift, by adding more vectors and parameters into the model (see Appendix B). The least-square estimates of $\hat{\boldsymbol{\beta}}_r$ and $\hat{\boldsymbol{\beta}}_i$ are $(\mathbf{X}^T\mathbf{X})^{-1}\mathbf{X}^T\mathbf{y}_r$ and $(\mathbf{X}^T\mathbf{X})^{-1}\mathbf{X}^T\mathbf{y}_i$, respectively. The activation level or the mean difference between the two states ($\bar{\mathbf{x}} - \boldsymbol{\mu}$) becomes $[\hat{\beta}_{r2} \quad \hat{\beta}_{i2}]^T$, which are the parameters of the reference waveform vector in real and imaginary axes. Setting the contrast ($\mathbf{v}$) to the reference waveform vector (i.e., $\mathbf{v} = [0 \quad 1]^T$), we calculate the covariance matrix of the contrast from the residual errors ($\hat{\boldsymbol{\varepsilon}}_r$ and $\hat{\boldsymbol{\varepsilon}}_i$) and the design matrix as follows:

$$\hat{\mathbf{S}}/n = \text{COV}(\hat{\boldsymbol{\varepsilon}}_r, \hat{\boldsymbol{\varepsilon}}_i)\mathbf{v}^T(\mathbf{X}^T\mathbf{X})^{-1}\mathbf{v}. \quad [8]$$

This closely resembles the variance of a contrast in a 1D GLM test whose value is $\hat{\sigma}^2\mathbf{v}^T(\mathbf{X}^T\mathbf{X})^{-1}\mathbf{v}$ (17). With these values calculated from the GLM method, the T^2 value can be obtained as follows:

$$T^2 = \mathbf{v}^T[\ \hat{\boldsymbol{\beta}}_r \quad \hat{\boldsymbol{\beta}}_i\ ]\cdot[\text{COV}(\hat{\boldsymbol{\varepsilon}}_r, \hat{\boldsymbol{\varepsilon}}_i)\mathbf{v}^T(\mathbf{X}^T\mathbf{X})^{-1}\mathbf{v}]^{-1}\cdot[\ \hat{\boldsymbol{\beta}}_r \quad \hat{\boldsymbol{\beta}}_i\ ]^T\mathbf{v}. \quad [9]$$

The *P*-value is found from Eq. [6] with $m = 2$.

MATERIALS AND METHODS

Simulated Data Analysis Using the Complex Data Analysis Method

Four different data sets of the complex data (no contrast, contrast in magnitude, contrast in both magnitude and phase, and contrast in phase) were generated to validate the proposed complex data analysis method. Each complex data set was generated by Eq. [10] with the proper SNR and contrast-to-noise ratio (CNR) values:

$$\mathbf{y} = \mathbf{X}(\boldsymbol{\beta}_r + i\boldsymbol{\beta}_i) + \mathbf{n}_r + i\mathbf{n}_i, \quad [10]$$

where $\mathbf{y}$ (a complex 50×1 vector) is a voxel time-series with 50 points, $\mathbf{X}$ is the same design matrix as in Eq. [7], the reference waveform vector ($\mathbf{h}$) of $\mathbf{X}$ is a boxcar block design with a duration of 10 samples, $\mathbf{n}_r$ and $\mathbf{n}_i$ are real 50×1 vectors distributed by $N(0,1)$, and $\boldsymbol{\beta}_r = [\beta_{r1} \quad \beta_{r2}]$ and $\boldsymbol{\beta}_i = [\beta_{i1} \quad \beta_{i2}]$ are the parameters in the real and imaginary axes, respectively. Since the noise is normalized, the parameters β_{r1} and β_{i1} represent the SNRs in the real and imaginary axes, whereas β_{r2} and β_{i2} represent the CNRs in the real and imaginary axes. The absolute values of the complex data were used to generate the magnitude data. We analyzed the magnitude data using the GLM method with the same design matrix ($\mathbf{X}$) to compare the results. A total of 100,000 voxels were simulated in each data set. The SNRs were set to 10 (i.e., $\beta_{r1} = \beta_{i1} = 10$). The first data set was Gaussian noise data with $\beta_{r2} = \beta_{i2} = 0$. This test was intended to show that the null hypothesis is not rejected when no activation exists. The second data set ($\beta_{r2} = \beta_{i2}$, both simulated at increasing values from 0 to 1.4) was generated to simulate the case in which the contrast exists only in magnitude. In the third data set the same contrast existed both in magnitude and phase ($\beta_{r2} = 0$ whereas β_{i2} increased from 0 to $1.4\sqrt{2}$). For the last data set, β_{r2} was changed from 0 to 1.4, while β_{i2} was kept as the opposite sign of β_{r2} to simulate the activation approximately in phase with the same amount of the complex contrast as in the previous two data sets.

Experimental Data Acquisition

All experiments were performed on a 1.5 T GE EXCITE system (40 mT/m and 150 mT/m/ms) with a 3-inch receive-only surface coil, except for a high-resolution reference scan that was acquired using an eight-channel head coil (MRI Devices Corp., USA). Five subjects, who provided written consent (approved by Stanford University), were immobilized by pads and instructed to avoid any voluntary motions. A high-resolution reference scan (spoiled gradient-echo (SPGR), FOV = 22 cm, resolution = $1 \times 1 \times 1$ mm³, TR = 11.7 ms, TE = 5.1 ms, flip angle = 25°, number of excitations (NEX) = 3) that covered the entire brain was acquired using the head coil on a separate day. In the main experiments using the surface coil, an axial slab (2-cm thickness) of the lower occipital lobe was targeted after the brain was localized with a 3D localizer sequence. An intermediate-stage anatomical scan (SPGR, FOV = 16 cm, resolution = $1 \times 1 \times 1$ mm³, TR = 12 ms, TE = 4.2 ms, flip angle = 25°, NEX = 6) that helped to realign the high-resolution reference scan to the functional

data was performed at the same resolution and FOV as in the functional scans. To identify the locations of large vessels, a 3D spiral trajectory high-resolution venogram (GRE, FOV = 16 cm, resolution = $0.5 \times 0.5 \times 1$ mm^3, TR = 70 ms, TE = 40 ms, flip angle = 25°, NEX = 12) was obtained by using a flow-compensated venogram (21) sequence. Linear shimming was targeted at the occipital lobe of the brain by a custom targeted shim program before the functional scans. For the functional studies, a 3D stack-of-spirals sequence (bSSFP, FOV = 16 cm, resolution = $1 \times 1 \times 1$ mm^3, TR = 15 ms, TE = 1.5 ms, flip angle = 5°, number of interleaves = 10, 18 slices for subjects 1–3 and 16 slices for the others) was utilized to cover a 3D volume every 3 s (Fig. 1c). Three different center frequencies (Δf_{center} = 0 Hz, –3 Hz, and 3 Hz) were scanned consecutively to cover the wider off-resonance frequencies. The stimulus was a 10-Hz contrast-reversing annulus grating flashing (15 s on and 15 s off, starting with a 15-s resting period). The subjects were instructed to gaze at cross-hairs located at the center of the visual stimulus and to breathe naturally. To ensure a steady state, the first 3D volume of the functional scan was discarded. Each functional scan lasted for 2 min 18 s.

Experimental Data Analysis

All functional data were inspected for subject motion. The third scan (Δf_{center} = 3 Hz) of subject 4 and the second and third scans (Δf_{center} = –3 Hz and 3 Hz) of subject 5 showed significant movements (>1 mm) and were therefore discarded from further analysis. A small shift (one voxel) between the functional scans was found in subject 3, which was fixed by aligning the data to the first functional scan. The intermediate-stage anatomical images were also aligned to the first functional scan. The signal attenuation in this intermediate-stage anatomical image, induced by the surface coil sensitivity, was removed with the use of a custom program. The high-resolution reference scan was then aligned to the intermediate-stage anatomical data using SPM5 (22). The alignment was further refined manually. The gray matter (GM) regions were identified from the reference scan. The venogram result was aligned to the high-resolution reference scan. We identified the locations of large veins from both the magnitude and phase venogram results by carefully tracking the vessel geometries from all of the slices. To display the results, the reference scan and z-score maps were enlarged to match the resolution with the venogram.

The magnitude and phase data were generated from the complex functional data. The phase data were unwrapped in the time-series for each voxel and 2π was added to make positive-signed data. After that, both data sets were processed individually to create "magnitude-only" and "phase-only" z-statistics maps using FEAT FSL (23). For these null-hypothesis tests, the noise should be assumed to be Gaussian. This assumption becomes valid in both magnitude and phase when the SNR is high (8). With the exception of high-pass filtering (cutoff frequency = 0.022 Hz), no other prestatistical process was performed. Unthresholded z-statistics maps were generated from FEAT based on each voxel. Since the negative correlations were meaningful, the thresholds were set on both the

positive and negative sides of the z-score distribution with a two-tailed P-value of 0.01. After thresholding, isolated activations in the positive and negative z-statistics maps were removed separately. Finally, the absolute values of the z-statistics maps were used to generate the activation maps. These activation maps were further masked by the mask generated in the magnitude-only data (10% thresholding, FEAT) with the skull area removed. The single-frequency acquisition analysis was performed on the data whose center frequency shift (Δf_{center}) was equal to 0 Hz. In the multifrequency acquisition analysis that combined the three different center frequency results using the maximum z-score projection method (5), the threshold was increased to $P < 0.005$.

For the complex data analysis, the functional data were decomposed into real and imaginary time-series. Slow signal drift was then removed by the same filter that was used previously. In each voxel the T^2-value was calculated from Eq. [9] as described in the Theory section. The reference waveform vector for the design matrix was the convolution of the stimulus pattern and a delayed-Gamma function that was generated by FEAT (the same waveform vector as that in the magnitude and phase analyses). The P-value was calculated in each voxel from the F-distribution (Eq. [6]), and the activation maps were generated by thresholding with a one-tailed P-value of 0.01 for the single-frequency acquisition analysis. After thresholding, we converted the P-values into z-scores by finding the equal probability in the one-tailed Gaussian distribution $N(0,1)$ for the color-coded activation maps. Isolated activations were removed from the activation maps and the results were masked using the same mask used in the magnitude and phase activation maps. After calculating the activation maps for each run, we combined the three different center frequency scans using the maximum z-score projection. The same threshold ($P < 0.005$) that was used in the magnitude and phase multifrequency acquisition analysis was utilized to threshold the activation maps before the projection.

RESULTS

The simulation results are shown in Fig. 2. When there is no activation, the complex-data analysis method results in the $N(0,1)$ distribution as shown in the normalized z-score histogram (Fig. 2a). In Figs. 2b–d, the power of the magnitude and complex data analysis methods is shown. The y-axis shows the percentage of the voxels that are classified as activations by the same threshold ($P < 0.01$) used in the experimental analysis. When the contrast is only in magnitude (Fig. 2b), the magnitude-data analysis method performs slightly better than the complex-data analysis method. However, the magnitude-data analysis method fails when the contrast is only in phase (Fig. 2d). When the contrast exists in both magnitude and phase (the same amount in both directions), the complex-data analysis method performs better than the magnitude-data analysis method. A more detailed analytic analysis of the performance of the two methods is given in the Discussion section. For the same contrast level in the complex domain, the complex-data analysis method shows the same power for the different contrast directions.
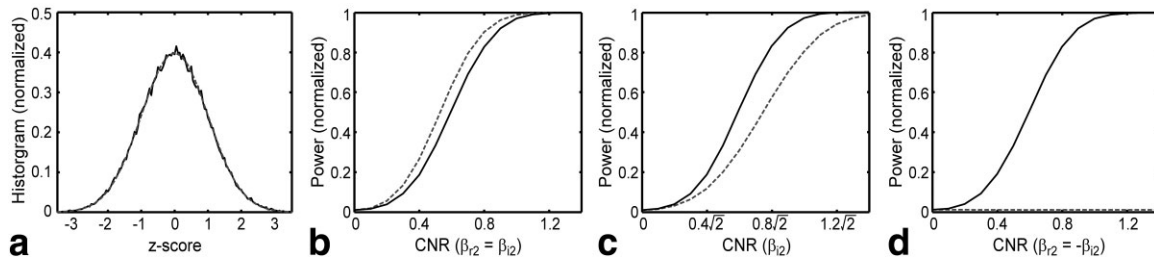
FIG. 2. Simulation results. **a:** Histogram of *z*-scores when there is no contrast (solid: simulation result; dashed: *N*(0,1)). Performance comparisons between the complex data analysis (solid) and the magnitude data analysis (dashed): (**b**) when the contrast is in magnitude, (**c**) when the contrast is in both magnitude and phase, and (**d**) when the contrast is in phase are shown.

The experimental results reported in the following paragraphs refer to subject 1 (the results from all five subjects are summarized in Table 1). Figure 3a and b reveal the activation maps from the single-frequency acquisition. The red-to-yellow colors show the magnitude activation, and the blue-to-light-blue colors show the phase activation. The voxels that contain both magnitude and phase activations are color-coded in green. Generally, activated voxels follow the sulcal areas and match the GM regions in the brain. Using the same threshold ($P < 0.01$), both magnitude and phase activation maps show a large number of significant activations. In the entire 3D volume, the magnitude activation maps contain 1758 activated voxels with a mean *z*-score of 3.75, and the phase activation maps contain 1700 voxels with a mean *z*-score of 3.71. As can be seen from the figures, a significant number of voxels (2576 voxels out of 3017 voxels that reveal either magnitude or phase activation) show the magnitude-only or phase-only activation, which proves that neither of them fully exploits the acquired data. The magnitude and phase time-series of the maximum *z*-scores (magnitude-only, phase-only, and both) from the third slice are shown in Fig. 3c–h. The time-series illustrate clear correlations between the stimulus (red bars) and the magnitude and/or phase data. Averaged over all slices, the activated voxels in the magnitude-data analysis show, on average, a 9.5% signal level change (a maximum 44.7% signal level change with $z = 9.20$). In the phase-data analysis the mean activation signal change is 0.107 radian (maximum 0.483 radian with $z = 8.26$).

Figure 4 shows three activation maps from a single slice that was scanned at three different center frequencies ($\Delta f_{center} = -3$, 0, and 3 Hz). Depending on the center fre-

quency, the locations of the activated voxels change and the commonly activated voxels show different levels of functional contrast. In some voxels the functional contrast shifts from the magnitude time-series to the phase time-series (or to both time-series) and vice versa. These results demonstrate that the contrast changes as a function of off-resonance frequency of the voxel (f_{off}), and the phase activation can be detected depending on the off-resonance frequency of the voxel.

The maximum *z*-score projected phase activation maps ($P < 0.005$) from the three scans reveal high *z*-score voxels near the veins (highlighted in yellow) that can be identified from the venogram (blue circles in Fig. 5). However, the GM regions that are not identified as veins also show statistically significant phase activations (circled in green). This result indicates that the sensitivity of phase activation measurement is greater than that of the venogram at the given resolution ($0.5 \times 0.5 \times 1$ mm³). The mean *z*-score of the maximum projected phase activation maps is 4.03, and the average signal change is 0.132 radian. A total of 2306 voxels are detected in the phase activation maps. These numbers are comparable to those of the maximum *z*-score projected magnitude activation maps ($P < 0.005$), which show a mean *z*-score of 4.01 and 2521 activated voxels.

In Fig. 6 the activation maps of the same slices from the magnitude, phase, and complex data (single-frequency) analyses are shown. The activation maps ($P < 0.01$) from the complex data analysis cover areas (circled in blue) that are missing in the magnitude data analysis results. In most of these areas the significant activations are found on the phase activation maps, proving that the complex data analysis method includes the activated voxels from both mag-

Table 1
Summary of Results From All Subjects

	Subject 1	Subject 2	Subject 3	Subject 4	Subject 5
Number of activated voxels: magnitude	1758	1317	773	2178	1429
Number of activated voxels: phase	1700	1107	592	1999	2128
Number of activated voxels: magnitude and phase	441	367	76	661	436
Number of activated voxels: complex	2989	2156	1291	3207	3099
Mean magnitude change (%)	9.5	10.4	8.3	8.5	9.5
Maximum magnitude change (%)	44.7	62.4	46.6	60.3	39.1
Mean phase change (radians)	0.107	0.131	0.100	0.095	0.108
Maximum phase change (radians)	0.483	0.781	0.711	0.692	0.545
SNR	12.3	11.7	12.1	13.4	12.1
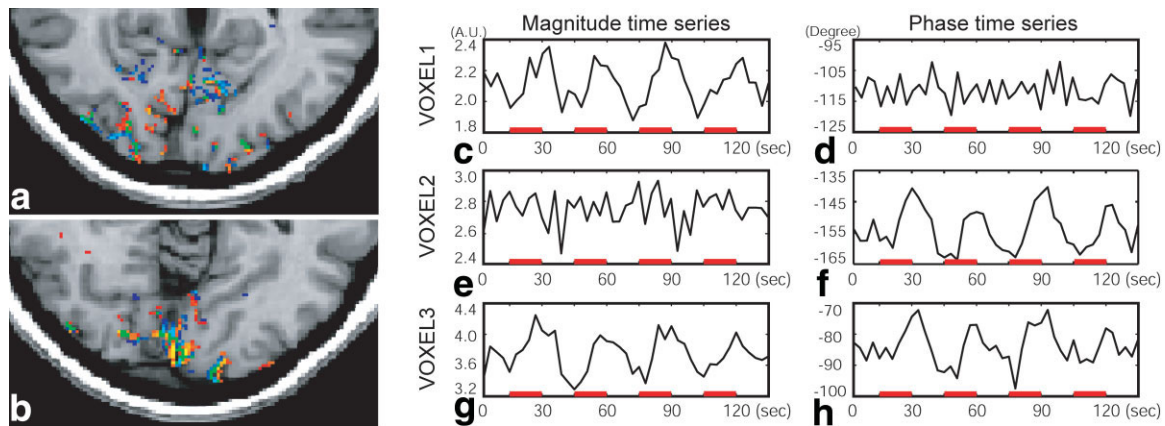
FIG. 3. Magnitude and phase-data analysis results. **a** and **b:** Activation maps from a single-frequency acquisition study ($\Delta f_{center} = 0$, $P < 0.01$). Red-to-yellow colors show the magnitude activations, and blue-to-light-blue colors show the phase activations. A voxel with both activations is color-coded in green. **c** and **d:** The time-series of a voxel with magnitude-only activation (x-axis, y-axis, slice) = (86,64,3). **e** and **f:** Phase-only activation (x-axis, y-axis, slice) = (83,61,3). **g** and **h:** Both magnitude and phase activations (x-axis, y-axis, slice) = (67,69,3). The red bars in the plots show the stimulated periods. The magnitude scale is represented as an arbitrary unit (A.U.).

nitude- and phase-signal changes. The complex activation maps contain 1.7 times more activated voxels (2989 voxels with a mean z-score of 3.60) than the magnitude activation maps (1758 voxels), as well as 1.8 times more activated voxels compared to the phase voxels (1700 voxels). This result demonstrates that in transition-band SSFP fMRI, the magnitude data analysis does not provide the full functional contrast contained in the data, whereas the complex data analysis provides better activation maps that include both magnitude and phase signal activations.

The maximum z-score projected activation maps from the complex-data analysis are shown in Fig. 7 (six slices out of 18 slices). The resulting activation maps provide wider spatial coverage compared to the single-frequency acquisition results (3783 voxels compared to 2989 voxels in the single-frequency analysis even after the threshold was increased).

DISCUSSION

Task-Correlated Phase-Signal Change

In this study we observed the expected task-correlated phase-signal change in a transition-band SSFP fMRI experiment using a 3D high-resolution ($1 \times 1 \times 1$ mm³) acquisition. A significant difference compared to previous low-resolution studies is that large task-correlated signal

changes were observed in both magnitude and phase. The magnitude results were similar in range to those reported in Ref. 6; however, the large phase-signal change and the large number of voxels that showed significant phase-signal changes were observed for the first time, to our knowledge, in the transition-band SSFP fMRI experiment.

To further validate these signal change levels, we performed a simulation using Eqs. [1]–[3]. The field strength was assumed to be 1.5T and the parameters for the SSFP profile were TR = 15 ms, TE = 7.5 ms, flip angle = 5°, T_1 = 780 ms, and T_2 = 80 ms (similar to GM). Two different voxels, each modeled by simple vessel geometries described below, were used. The first voxel was assumed to have one large cylindrical vein that was tilted by $\pi/6$ to the main field and occupied 50% of the voxel volume. The fractional oxygen saturation of hemoglobin (Y) was changed from 0.61 to 0.73 between the activation state and baseline state. The vessel showed a 2.2-Hz frequency shift, and the maximum signal changes were approximately 50% in magnitude and 0.60 radian in phase (the intravascular part). The resulting activation profiles are shown in Fig. 8a. The second voxel was a spherical voxel (1 mm³) consisting of small cylindrical veins (4 μm radius) that were uniformly distributed according to the density $P(\theta) = 0.5\sin\theta$, $-\pi < \theta \leq \pi$, (24) and occupied 2% of the voxel volume (400 veins) with Y changing from 0.77 to 0.85 (Y
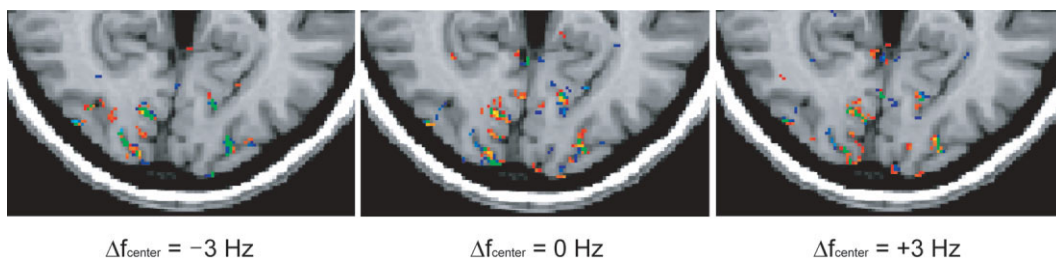
FIG. 4. Results from the different center frequencies (Δf_{center} = −3, 0, and 3 Hz). In each center frequency a voxel shows different levels of functional contrast. Moreover, the functional contrast shifts from the magnitude to the phase and vice versa (or exists in both). See Fig. 3 for the color-coding scheme.

FIG. 5. Phase activation maps and venogram results. **a** and **c**: Phase activation maps from the maximum *z*-score projection. **b** and **d**: Magnitude images from the high-resolution venogram. The vein locations (highlighted in yellow) are identified from both magnitude and phase images by tracking veins from all slices. The blue circles are the areas where the phase activation is primarily from the vein locations, while the green circles represent the GM regions that are not identified as veins in the venogram.
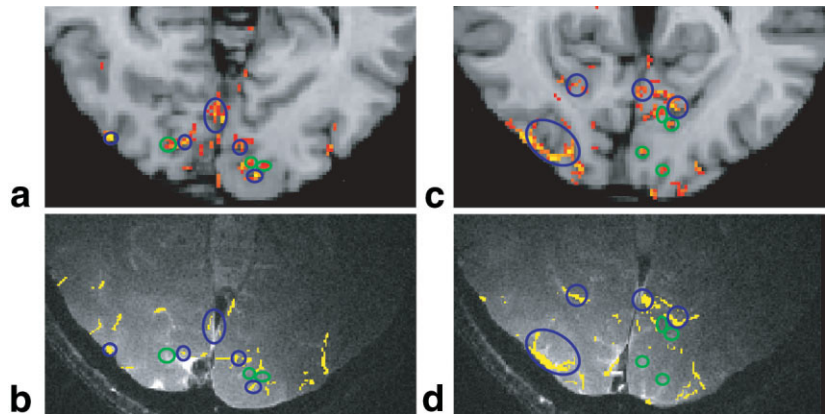
values from Ref. 25). This voxel (capillary voxel) showed a ~2% magnitude change near the resonance frequency and a ~0.013 radian phase change near the curves of the phase transition band (Fig. 8b). These simulation results agreed approximately with the experimental results in the sense that the maximum signal change levels in the experiments were similar to the simulation results of the single large vein case, whereas the mean signal change levels were relatively close to (and higher than) the results of the small veins, which mimic a voxel with capillary geometry (see Table 1 for the experimental results).

Another interesting aspect of the simulation results is that the magnitude and phase revealed different activation levels at different off-resonance frequencies. The single large vein case showed the maximum magnitude peak at -0.1 Hz with a smoother contrast change in the positive off-resonance side, while the phase contrast peaked at -0.9 Hz with a smoother change on the negative side. In the capillary geometry case, the magnitude showed a peak signal change close to the 0 Hz off-resonance frequency when the phase showed almost no contrast. Meanwhile, the phase showed biphasic maximum signal changes near ±2.2 Hz. These discrepancies in the magnitude- and phase-signal activations were also clearly observed in the activation maps (Fig. 3), where only a fractional portion of voxels showed both magnitude and phase activations while others showed either magnitude or phase activation. To identify the magnitude and phase activation level dependency on the off-resonance frequency, a more careful analysis based on a high-resolution field map and more realistic voxel properties must be performed. Moreover, one should be cautious in interpreting the results since the

magnitude and phase contrast profiles largely depend on the voxel properties, which can vary from one voxel to another.

Figure 9 illustrates the simulation results of the TE dependency of the magnitude and phase activations. Two different voxels were simulated: one (1 mm³) with a cylindrical vein (radius = 60 μm, *Y* changing from 0.61 to 0.73, parallel to the main field), and one with the capillary geometry described in the previous simulation. Other parameters were also the same. The maximum magnitude and phase activation levels were plotted over TE = 0 to TR. As TE increased, the magnitude activation results showed an increase of the activation level, whereas the phase activation showed a slight decrease. These changes originated from the nonlinearity of the SSFP magnetization profile at different TEs, as shown in Fig. 1a and b. The most important observation here is that high functional contrast exists even at TE = 0 in SSFP fMRI. Moreover, the contrast level is relatively uniform throughout the readout period because magnetization profiles change little over different TEs. This is especially true in the phase profile near the resonance frequency where most of the phase functional contrast is generated (Fig. 1b). These results were expected and are considered to be a major benefit of SSFP fMRI, since it does not require a long TE to acquire contrasts (5).

More simulation results to elucidate the nature of the phase-signal change are shown in Fig. 10. First, the intra- and extravascular phase activation levels at different vessel orientations are plotted over a range of off-resonance frequencies (Fig. 10a and b). A vein (radius = 60 μm, *Y* changing from 0.61 to 0.73) was simulated for eight differ-
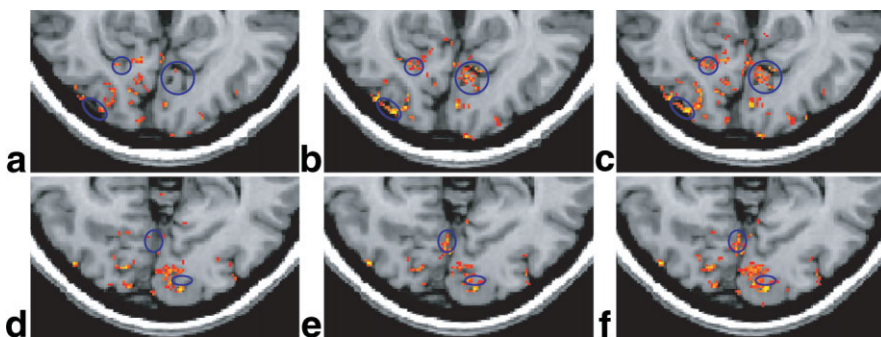
FIG. 6. Magnitude (**a** and **d**), phase (**b** and **e**), and complex (**c** and **f**) activation maps from the same slices. The complex data analysis results cover areas (circled in blue) that are missing in the magnitude activation maps. In these areas significant activations can be found in the phase activation maps.
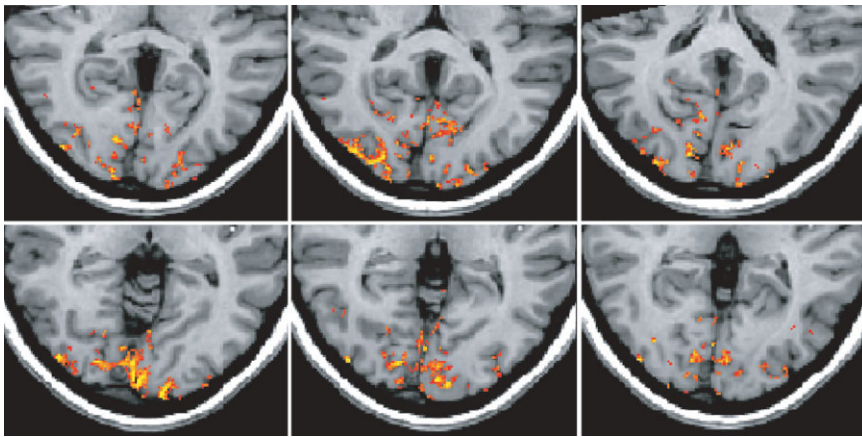
FIG. 7. Maximum *z*-score projected results in the complex data analysis. A total of six slices (slices 2, 5, 8, 11, 14, and 17 from bottom left to top right) from 18 slices are shown. A higher threshold ($P < 0.005$) is applied to reduce the false positives that are increased as a result of the maximum projection method.

ent angles ($0 \leq \theta \leq \pi$, where θ is an angle of the vein with respect to a B_0 field). All of the sequence parameters were the same as before (TE = TR/2). The intravascular phase signal decreased as the angle increased from 0 to 0.96 (rad) and became negative from 0.96 to $\pi/2$ (rad). In the extravascular case, the phase signal increased (both positively and negatively depending on the off-resonance frequency) as the angle increased from 0 to $\pi/2$. From $\pi/2$ to π, both intra- and extravascular phase activations reversed the patterns from 0 to $\pi/2$ (see Fig. 10a and b). These whole patterns repeated themselves as the angle increased from π to 2π. In Fig. 10c, the maximum activation level and full width at half maximum (FWHM) off-resonance coverage of the intravascular phase signal are shown over a range of field strengths. The simulation parameters were the same as in the vessel orientation simulation, except that the vein was parallel to the main field, and the field strength was increased from 0.5T to 7T. One observation from these results is that the intravascular phase-signal change begins to saturate as the field increases. This is because the phase transition provides a π phase shift over a narrow frequency band. Once the frequency shift (Δf) becomes larger than this band, the phase change becomes saturated. Therefore, the increased frequency shift (Δf) at higher field strengths (>4T) does not contribute proportionally to the phase-signal change. Only the off-resonance coverage increases approximately linearly over the field strengths. However, since the intravascular frequency shift is a function of a vessel orientation (Eq. [1]), the saturation of the phase activation will start at a higher field strength in other vessel orientations. Moreover, the contributions from the extravascular frequency shift will also have different saturation patterns. In the capillary case, the oxygen concentration change (Y) is smaller than that of the vein, resulting in smaller intravascular frequency shifts that in turn reduce the saturation effect.

One criterion for including the phase-signal change in the activation map is that it must show functionally localized signals. In a study by Menon (2), the source of the phase-signal change was assumed to originate primarily from the large veins. As a result, the phase-signal change was not included, but rather was utilized to suppress the large vein signals. In his experiment the data were collected at 4T, where (theoretically) the bulk frequency shift is 2.7 times greater than it is at 1.5T. However, the phase changes in Ref. 2 (0.085 radian in visible veins and 0.028 radian in other activated voxels) appear to be smaller compared to our results (a maximum 0.482 radian phase change with 0.107 radian, on average, in the single-frequency analysis), presumably because the phase change is much greater in transition-band SSFP fMRI due to the sharp phase transition band, and also because we employed a smaller voxel size.

As also mentioned in Ref. 2, the minimum detectable phase change depends on the SNR. In our experiment the SNR measured in the nonactivated voxels ($|z| < 0.67$) was 12.3 within the mask (roughly covering the brainstem to the back of the brain) with a single-pixel, temporal-phase SD of 0.114. Hence, the minimum detectable phase change in our experimental setting ($P < 0.01$ and $n = 45$) was 0.041 radian. This minimum threshold agrees with the histogram result of the signal changes from the phase activation voxels whose minimum detected signal level was 0.031 radian (Fig. 11). These results are still greater than the simulation result (a 0.013 radian change in the capillary geometry), but are not substantially different. Hence, it is plausible that the phase activation would provide a certain degree of localized information. Moreover, it has been suggested that at 1.5T most of the magnitude signal changes originate from larger veins than capillaries (26). These results, together with the aforementioned venogram results and the fact that the number of
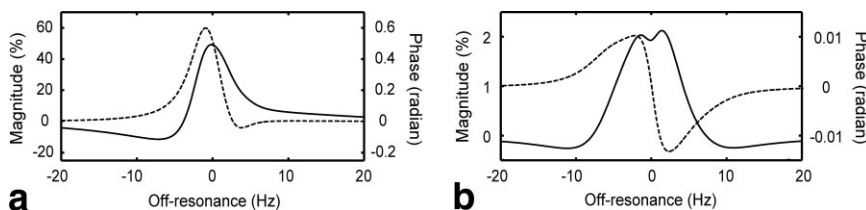
FIG. 8. Simulation results of the magnitude (solid line) and phase (dashed line) contrasts depending on the off-resonance frequency. **a:** A voxel with a large vein (radius = 0.4 mm) case. **b:** A voxel with 400 small veins (radius = 4 μm) distributed by 0.5 sin(θ).

FIG. 9. Simulation results of the maximum (**a**) magnitude and (**b**) phase activations at different TEs. The solid lines show the results from a voxel with a single vein (60 μm), and the dashed lines show a voxel with the capillary geometry described in the text. Unlike conventional fMRI, large functional contrasts (both in magnitude and phase) exist even at early TEs.
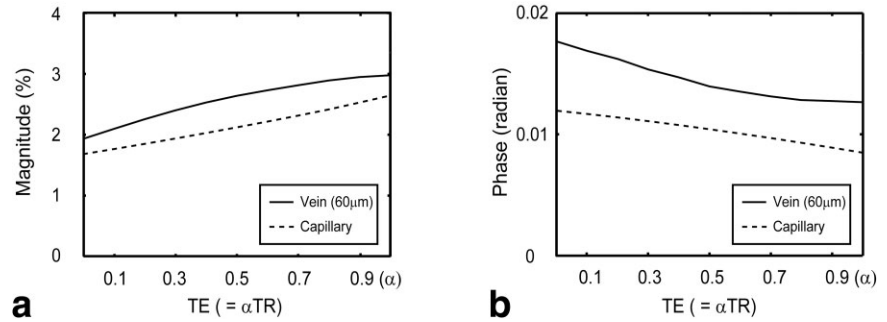
phase-activated voxels was comparable to the number of magnitude-activated voxels (which can be interpreted to mean that the sensitivity of the phase activation is similar to the sensitivity of the magnitude), indicate that for the proposed method it may be beneficial to include the phase-signal change in the activation maps.

There are several ways to improve the minimum detection threshold. First, one can increase the total acquisition time to increase the statistical power. Since our experiment was relatively short (2 min 15 s), increasing the total scan time by a factor of 4 (9 min) is still a reasonable approach. Another method is to use a higher-field-strength system. The bulk frequency shift of vessels increases linearly with the field strength, resulting in increased phase-signal changes. In addition to this increased contrast, the SNR also increases linearly, resulting in a quadratic increase of the detectability. A third method is using a real-time, respiration-compensation technique. Lee et al. (27) demonstrated a significant increase in the *z*-score by reducing the respiration-induced the SSFP profile shift. This respiration compensation is especially effective for increasing the contrast and reducing the noise interference because the respiration-induced B_0 field modulates the SSFP transition profile, causing a large signal interference and time-varying functional contrasts in transition-band SSFP fMRI. By combining these methods, one can obtain much more localized activation information from the phase signal, which makes the proposed complex data analysis method more beneficial for transition-band SSFP fMRI.

Since both phase and magnitude signal changes are greater in large veins, both the complex- and magnitude-data analyses will show greater signal changes in the veins. However, the signal changes from large veins are usually of no interest because they impede the localization ability of high-resolution studies. Therefore, it is desirable to remove these large signal changes from the activation maps. This can be done with the use of diffusion-weighted suppression techniques that remove intravascular signals using bipolar diffusion gradients (26,28,29), a time-series based analysis that identifies the large veins based on the time-series of a voxel (30), or a venogram approach (31). Once the large vein signals are removed, the complex-data analysis method will provide greater benefits by including more localized brain activations in the analysis.

Complex Data Analysis Method

When written in polar coordinates, the magnitude and phase contrasts are orthogonal to each other; therefore, a univariate test designed for testing changes in magnitude, by definition, will be insensitive to changes in phase. A change that occurs in magnitude and phase simultaneously can only be captured fully by a complex bivariate test. On the other hand, if the effect truly exists only in the magnitude, the magnitude-only test will have more power. This is because in order to prevent false positives in the direction of the phase, the complex test allocates a null probability mass in that direction, which is wasted if the change occurs only in the magnitude. As a result, the magnitude-only test yields a relatively lower threshold (and therefore higher power) for the same significance level. This explains the simulation described in the Results section, in which the complex-data analysis outperformed the magnitude data analysis except when the contrast existed strictly in magnitude. A mathematical analysis of the performance of the two methods is presented in Appendix A. The performance of the analysis methods
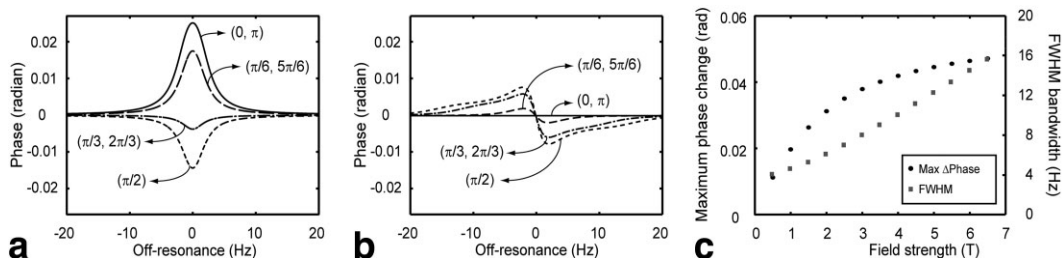
FIG. 10. Simulation results of the phase activations at different vessel orientations and field strengths: (**a**) intravascular and (**b**) extravascular phase-signal changes over 0 to π radian, and (**c**) maximum intravascular phase change (circle) and its FWHM off-resonance frequency coverage (rectangle) at different field strengths.
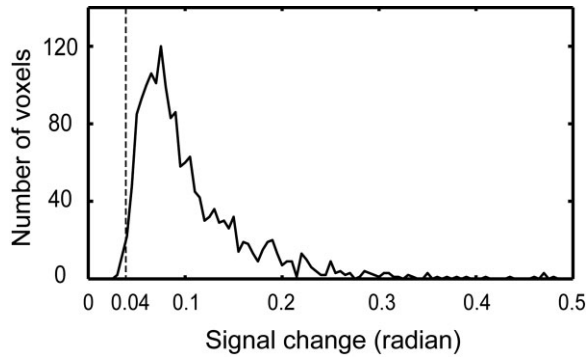
FIG. 11. Histogram of the phase-signal change from the phase-activated voxels. The dashed line (0.04 radian) shows the minimum detectable phase-signal change from the mean SD in the experiment.

was measured by the required SNR to detect a certain contrast level at a given probability of detection (P_D) and probability of false alarm (P_{FA}). Figure 12a and b show the patterns of the required SNR (in log scale) for $P_{FA} = 0.01$ and $P_D = 0.99$ in the magnitude and complex data analysis methods, using Eqs. [A1] and [A2]. The dark red straight band in Fig. 12a shows that it requires very high (or infinite) SNR to detect the contrast in the phase direction by the magnitude data analysis method, as expected from the simulation (Fig. 2d). The required SNR pattern for the complex data analysis method is angularly symmetric, representing the same performance for the same amount of contrast in the complex domain. Figure 12c shows the required SNR difference (in log scale) between the complex and magnitude data analyses (Eq. [A3]). The required SNR for the magnitude data analysis is higher than that of the complex data analysis for most of the contrasts except for the dark blue areas (29% of the total plane) between the dashed white lines, where the contrasts are primarily aligned in the magnitude direction. This result indicates the superiority of the complex data analysis for most of the contrasts, which was also observed in the simulation and experimental results (Figs. 2 and 6). Even in the dark blue areas, the maximum required SNR difference is only 0.69 dB, indicating a very small difference in the performance of the two methods.

The proposed complex data analysis can be intuitively understood as follows: If the noise is assumed to be distributed as a 2D Gaussian with $N(0,\sigma^2\mathbf{I})$, where $\mathbf{I}$ is a 2×2 identity matrix, $\hat{\mathbf{S}}^{-1}$ (in Eq. [4]) becomes $\mathbf{I}/\sigma^2$. In this case the T^2 value becomes proportional to $(\bar{\mathbf{x}} - \boldsymbol{\mu})^T(\bar{\mathbf{x}} - \boldsymbol{\mu})$, which can be seen as the distance between the sample

mean vector and the population mean vector in a complex plane. In other words, if one uses a simple boxcar model, ignoring the transients of the hemodynamic response function, the signal level difference (or contrast) in fMRI data can be defined as the distance between the mean vector of the activation state and the mean vector of the baseline in the complex plane.

In Appendix B a theoretical proof is given to demonstrate that our complex data analysis method is equivalent to the GLRT method (9) when the design matrices are the same for the magnitude and phase. One of the advantages of our method is that it is computationally efficient. Since it is based on the T^2-test with the GLM method, the computational time for a sample data took only 2.4 times longer compared to the magnitude data analysis. On the other hand, the GLRT method requires iterations in each voxel to search for the optimum parameter values, which can potentially lead to a non-negligible increase in computational time for fMRI data.

Future Work

In addition to the bulk frequency shift, the BOLD effect includes a T_2 change that originates from the protons diffused by red blood cells (intravascular) and the microgradients between the vessel and the surrounding tissue (extravascular). In SSFP-based fMRI, this T_2 change can modulate the magnetization profile of bSSFP. A voxel with large veins can experience a T_2 on the order of a 10% change primarily from the intravascular effect, whereas the T_2 change in the GM is negligible due to the small volume of blood at 1.5T (25,32). At higher field strengths, however, the increased extravascular effect can make the T_2 change significant in the GM. Therefore, it is important to consider the profile modulation from the T_2 change as a source of the functional contrast at higher field strengths.

Another possible application of the proposed complex data analysis is conventional GRE-based fMRI in high-field experiments. At high field strengths ($\geq$ 7T), where T_2^* shortening is significant in large veins (29), the phase-signal change from the GM will show a higher signal correlation compared to that obtained at a lower field strength. In this case the proposed complex-data analysis method will be beneficial for detecting signal changes from both the magnitude and phase.

CONCLUSIONS

In this paper we have presented the results of an isotropic 1-mm resolution 3D (160 × 160 × 18 mm^3) transition-band
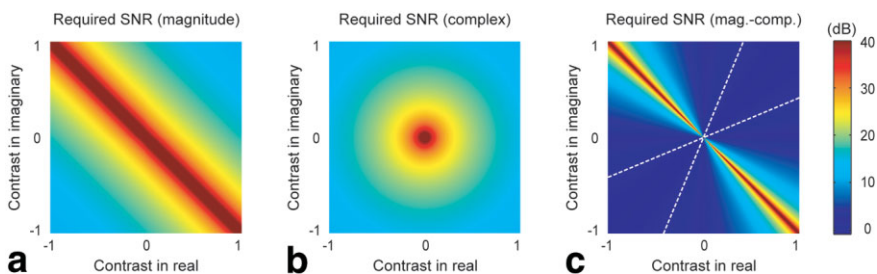
FIG. 12. Performance comparison between the magnitude data analysis and complex data analysis. The required SNR patterns (in log scale) for the (**a**) magnitude data analysis and (**b**) complex data analysis on the real and imaginary contrast planes. **c:** The required SNR difference between the magnitude and complex data analysis methods in log scale.

SSFP fMRI experiment. These high-resolution results provide both magnitude and phase data, depending on the off-resonance frequency and vessel properties of a voxel. To include both functional contrasts, a new complex data analysis method based on the T²-test is proposed. This method includes both magnitude and phase activations to compensate for the missing phase activations in the magnitude data analysis method. The method will provide more benefits at higher field strengths after large-vessel signals are removed. It can also be adopted in conventional fMRI analysis to include the task-correlated phase-signal change in high-resolution or high-field experiments.

ACKNOWLEDGMENTS

APPENDIX A

In this section we analyze the performance of the magnitude and complex data analysis methods in terms of the required SNR. To facilitate the presentation, the design matrix and the contrast are defined as $\mathbf{X} = [\mathbf{c}\ \ \mathbf{h}]$ and $\mathbf{v} = [0\ \ 1]^T$, where $\mathbf{c} = [\ 1\ \ 1\ \ \cdots\ \ 1\ ]^T/\sqrt{n}$, and the reference waveform vector ($\mathbf{h}$) follows

$$\sum_{k=1}^{n} h_k = 0 \quad \text{and} \quad \sum_{k=1}^{n} h_k^2 = 1.$$

With these scaling factors, the $\mathbf{X}^T\mathbf{X}$ becomes $\mathbf{I}$ (instead of $n\mathbf{I}$ when the sum of squares is n) and simplifies the derivations thereafter. The $\hat{\boldsymbol{\beta}}_1$ and $\hat{\boldsymbol{\beta}}_2$ are also scaled by a factor of $\sqrt{n}$, which removes the n terms in the magnitude and complex test statistics.

In the magnitude data analysis, the test statistic can be simplified as

$$t_1 = \frac{(\mathbf{v}^T\hat{\boldsymbol{\beta}})^2}{\text{var}(\mathbf{v}^T\hat{\boldsymbol{\beta}})} = \frac{\hat{\beta}_2^2}{\hat{\sigma}^2\mathbf{v}^T(\mathbf{X}^T\mathbf{X})^{-1}\mathbf{v}} = \frac{\hat{\beta}_2^2}{\hat{\sigma}^2},$$

where $\hat{\sigma}^2 = (\mathbf{y} - \mathbf{X}\hat{\boldsymbol{\beta}})^T(\mathbf{y} - \mathbf{X}\hat{\boldsymbol{\beta}})/df$, $\hat{\beta}_2 = |\hat{\beta}_{r2} + \hat{\beta}_{i2}|/2$ (the length of the magnitude contrast when the contrast is $\hat{\beta}_{r2}$ in real and $\hat{\beta}_{i2}$ in imaginary), df is the degrees of freedom, and all the other variables are defined as in the Theory section. The test statistic t_1 is distributed as a noncentral F-distribution with 1 and n–1 degrees of freedom, and the noncentrality parameter is

$$\lambda_1 = \frac{\beta_2^2}{\sigma^2}.$$

If $\mathbf{v}^T\boldsymbol{\beta} = \beta_2 = 0$, the distribution becomes central.

In the complex data analysis, the test statistic is given by

$$t_2 = \hat{\boldsymbol{\beta}}_2^T\hat{\mathbf{S}}^{-1}\hat{\boldsymbol{\beta}}_2.$$

To simplify the analysis, a case in which $\hat{\mathbf{S}} = \hat{\sigma}^2\mathbf{I}$ is considered. The test statistic can then be written as

$$t_2 = \frac{\hat{\boldsymbol{\beta}}_2^T\hat{\boldsymbol{\beta}}_2}{\hat{\sigma}^2}.$$

The normalized test statistic with a $\dfrac{n-2}{2(n-1)}$ normalization factor is distributed as a noncentral F with 2 and n–2 degrees of freedom with a noncentrality parameter:

$$\lambda_2 = \frac{\boldsymbol{\beta}_2^T\boldsymbol{\beta}_2}{\sigma^2}.$$

The performance of the magnitude and complex data analysis methods can be analyzed based on the required SNR to detect certain levels of contrasts at a given probability of detection (P_D) and probability of false alarm (P_{FA}). As mentioned above, the noncentrality parameters of both tests are a function of the noise variance and contrasts. On the other hand, this noncentrality parameter is determined by the prespecified P_D, P_{FA}, and the distributions (33). Therefore, the required SNR can be defined using this noncentrality parameter as shown below.

In the magnitude data analysis case, the required SNR becomes

$$\text{SNR}_{\text{req\_magnitude}} = \frac{c\beta_1}{\sigma} = \frac{c\beta_1}{\sqrt{\dfrac{\beta_2^2}{\lambda_1}}} = \frac{c\beta_1}{\sqrt{\dfrac{1}{\lambda_1}\dfrac{(\beta_{r2} + \beta_{i2})^2}{2}}}, \quad [\text{A1}]$$

where $c = 1/\sqrt{n}$.

In the complex data analysis case, it becomes

$$\text{SNR}_{\text{req\_complex}} = \frac{c\beta_1}{\sigma} = \frac{c\beta_1}{\sqrt{\dfrac{\boldsymbol{\beta}_2^T\boldsymbol{\beta}_2}{\lambda_2}}} = \frac{c\beta_1}{\sqrt{\dfrac{\beta_{r2}^2 + \beta_{i2}^2}{\lambda_2}}}. \quad [\text{A2}]$$

The performance difference is defined as

$$20\log(\text{SNR}_{\text{req\_complex}}) - 20\log(\text{SNR}_{\text{req\_magnitude}})$$

$$= 10\log\left[\frac{\lambda_2}{\beta_{r2}^2 + \beta_{i2}^2}\right] - 10\log\left[\frac{2\lambda_1}{(\beta_{r2} + \beta_{i2})^2}\right]. \quad [\text{A3}]$$

Figure 10c shows this performance difference on the contrast plane. To illustrate the required SNR patterns in each analysis method, $c\beta_1 (=\sqrt{(\beta_{r1}^2 + \beta_{i1}^2)/n})$ was set to 1 with β_{r2} and β_{i2} changing from –1 to 1 (Fig. 10a and b).

APPENDIX B

Here a mathematical proof is given to show the equivalence of the GLRT method (comparing H_a vs. H_d in Ref. 9) to the proposed complex data analysis method when the design matrices are the same for the magnitude and phase.

First, Eq. [7] is generalized to include arbitrary numbers of parameters:

$$\mathbf{y}_r = \mathbf{X}\boldsymbol{\beta}_r + \boldsymbol{\varepsilon}_r$$

$$= [\ \mathbf{x}_1 \quad \mathbf{x}_2 \quad \cdots \quad \mathbf{x}_L\ ][\ \beta_{r1} \quad \beta_{r2} \quad \cdots \quad \beta_{rL}\ ]^{\mathrm{T}} + \boldsymbol{\varepsilon}_r$$

$$\mathbf{y}_i = \mathbf{X}\boldsymbol{\beta}_i + \boldsymbol{\varepsilon}_i$$

$$= [\ \mathbf{x}_1 \quad \mathbf{x}_2 \quad \cdots \quad \mathbf{x}_L\ ][\ \beta_{i1} \quad \beta_{i2} \quad \cdots \quad \beta_{iL}\ ]^{\mathrm{T}} + \boldsymbol{\varepsilon}_i\ ,$$

where $\mathbf{x}_1, \mathbf{x}_2, \ldots, \mathbf{x}_L$ are real $n \times 1$ vectors representing such waveforms as a constant, a linear drift, and reference waveforms. The least-square estimates of the parameters and the contrast ($\mathbf{v}$) can be written as

$$\hat{\boldsymbol{\beta}} = [\ \hat{\boldsymbol{\beta}}_r \quad \hat{\boldsymbol{\beta}}_i\ ] = \begin{bmatrix} \hat{\beta}_{r1} & \hat{\beta}_{r2} & \cdots & \hat{\beta}_{rL} \\ \hat{\beta}_{i1} & \hat{\beta}_{i2} & \cdots & \hat{\beta}_{iL} \end{bmatrix}^{\mathrm{T}} \quad \text{and}$$

$$\mathbf{v} = [\ v_1 \quad v_2 \quad \cdots \quad v_L\ ]^{\mathrm{T}}.$$

Then the test statistic for the proposed complex data analysis becomes

$$t_2 = \mathbf{v}^{\mathrm{T}}\hat{\boldsymbol{\beta}}(\hat{S}/n)^{-1}\hat{\boldsymbol{\beta}}^{\mathrm{T}}\mathbf{v},$$

where

$$\hat{\boldsymbol{\beta}} = [(\mathbf{X}^{\mathrm{T}}\mathbf{X})^{-1}\mathbf{X}^{\mathrm{T}}\mathbf{y}_r \quad (\mathbf{X}^{\mathrm{T}}\mathbf{X})^{-1}\mathbf{X}^{\mathrm{T}}\mathbf{y}_i] \quad \text{and}$$

$$\hat{\mathbf{S}}/n = \mathrm{COV}(\hat{\boldsymbol{\varepsilon}}_r,\hat{\boldsymbol{\varepsilon}}_i)\mathbf{v}^{\mathrm{T}}(\mathbf{X}^{\mathrm{T}}\mathbf{X})^{-1}\mathbf{v}.$$

Assuming the case in which noise in the real and imaginary axes is independent, as assumed in Ref. 9, then $\mathrm{COV}(\hat{\boldsymbol{\varepsilon}}_r,\hat{\boldsymbol{\varepsilon}}_i) = \hat{\sigma}^2\mathbf{I}$ and $\hat{\sigma}^2$ can be defined as the mean of the real and imaginary variances:

$$2\hat{\sigma}^2 = \mathrm{var}(\hat{\boldsymbol{\varepsilon}}_r) + \mathrm{var}(\hat{\boldsymbol{\varepsilon}}_i) =$$

$$\left[\frac{1}{n-L}(\mathbf{y}_r - \mathbf{X}\hat{\boldsymbol{\beta}}_r)^{\mathrm{T}}(\mathbf{y}_r - \mathbf{X}\hat{\boldsymbol{\beta}}_r)\right]$$

$$+ \left[\frac{1}{n-L}(\mathbf{y}_i - \mathbf{X}\hat{\boldsymbol{\beta}}_i)^{\mathrm{T}}(\mathbf{y}_i - \mathbf{X}\hat{\boldsymbol{\beta}}_i)\right]$$

Then the T^2-test statistic becomes

$$t_2 = \frac{1}{\hat{\sigma}^2}\mathbf{v}^{\mathrm{T}}\hat{\boldsymbol{\beta}}[\mathbf{v}^{\mathrm{T}}(\mathbf{X}^{\mathrm{T}}\mathbf{X})^{-1}\mathbf{v}]^{-1}\hat{\boldsymbol{\beta}}^{\mathrm{T}}\mathbf{v}. \qquad [\mathrm{A4}]$$

In the GLRT case we are interested in distinguishing whether there is any activation in the magnitude and/or phase (i.e., H_a vs. H_d in Ref. 9). The test statistic is defined as the ratio of the probability density function (PDF) of the null and alternative hypotheses.

First, under the alternative hypothesis (H_a), the estimated log PDF of the signal is given by:

$$LLa = \log P(\mathbf{y}|H_a) = -n\log 2\pi\sigma_{H_a}^2$$

$$- \frac{1}{2\sigma_{H_a}^2}[(\mathbf{y}_r - \mathbf{X}\boldsymbol{\beta}_r)^{\mathrm{T}}(\mathbf{y}_r - \mathbf{X}\boldsymbol{\beta}_r) + (\mathbf{y}_i - \mathbf{X}\boldsymbol{\beta}_i)^{\mathrm{T}}(\mathbf{y}_i - \mathbf{X}\boldsymbol{\beta}_i)]$$

One can find the maximum likelihood estimates of the parameters by equating

$$\frac{\partial LLa}{\partial \boldsymbol{\beta}_r} = 0, \quad \frac{\partial LLa}{\partial \boldsymbol{\beta}_i} = 0, \quad \text{and} \quad \frac{\partial LLa}{\partial \sigma_{H_a}^2} = 0.$$

These equations lead to

$$\hat{\boldsymbol{\beta}}_r = (\mathbf{X}^{\mathrm{T}}\mathbf{X})^{-1}\mathbf{X}^{\mathrm{T}}\mathbf{y}_r$$

$$\hat{\boldsymbol{\beta}}_i = (\mathbf{X}^{\mathrm{T}}\mathbf{X})^{-1}\mathbf{X}^{\mathrm{T}}\mathbf{y}_i,$$

$$\hat{\sigma}_{H_a}^2$$

$$= \frac{1}{2n}[(\mathbf{y}_r - \mathbf{X}\hat{\boldsymbol{\beta}}_r)^{\mathrm{T}}(\mathbf{y}_r - \mathbf{X}\hat{\boldsymbol{\beta}}_r) + (\mathbf{y}_i - \mathbf{X}\hat{\boldsymbol{\beta}}_i)^{\mathrm{T}}(\mathbf{y}_i - \mathbf{X}\hat{\boldsymbol{\beta}}_i)].$$

The same results can be derived in the magnitude and phase domain that was used as the convention in Ref. 9.

Therefore, LLa can be simplified as

$$LLa = \log \hat{P}(\mathbf{y}|H_a) = -n\log 2\pi\hat{\sigma}_{H_a}^2 - n$$

Under the null hypothesis (H_d), we have

$$LLd = \log P(\mathbf{y}|H_d) = -n\log 2\pi\sigma_{H_d}^2$$

$$- \frac{1}{2\sigma_{H_d}^2}[(\mathbf{y}_r - \mathbf{X}\boldsymbol{\beta}_r)^{\mathrm{T}}(\mathbf{y}_r - \mathbf{X}\boldsymbol{\beta}_r) + (\mathbf{y}_r - \mathbf{X}\boldsymbol{\beta}_i)^{\mathrm{T}}(\mathbf{y}_i - \mathbf{X}\boldsymbol{\beta}_i)]$$

When we enforce the constraint $\mathbf{v}^{\mathrm{T}}\boldsymbol{\beta}_r = 0$ and $\mathbf{v}^{\mathrm{T}}\boldsymbol{\beta}_i = 0$, the constrained maximum likelihood estimates of the parameter vectors are given by (9,34):

$$\tilde{\boldsymbol{\beta}}_r = \hat{\boldsymbol{\beta}}_r - (\mathbf{X}^{\mathrm{T}}\mathbf{X})^{-1}\mathbf{v}[\mathbf{v}^{\mathrm{T}}(\mathbf{X}^{\mathrm{T}}\mathbf{X})^{-1}\mathbf{v}]^{-1}\mathbf{v}^{\mathrm{T}}\hat{\boldsymbol{\beta}}_r,$$

$$\tilde{\boldsymbol{\beta}}_i = \hat{\boldsymbol{\beta}}_i - (\mathbf{X}^{\mathrm{T}}\mathbf{X})^{-1}\mathbf{v}[\mathbf{v}^{\mathrm{T}}(\mathbf{X}^{\mathrm{T}}\mathbf{X})^{-1}\mathbf{v}]^{-1}\mathbf{v}^{\mathrm{T}}\hat{\boldsymbol{\beta}}_i.$$

When $\frac{\partial LLa}{\partial \sigma_{H_d}^2} = 0$, we have

$$\tilde{\sigma}_{H_d}^2 = \frac{1}{2n}[(\mathbf{y}_r - \mathbf{X}\tilde{\boldsymbol{\beta}}_r)^{\mathrm{T}}(\mathbf{y}_r - \mathbf{X}\tilde{\boldsymbol{\beta}}_r)$$

$$+ (\mathbf{y}_i - \mathbf{X}\tilde{\boldsymbol{\beta}}_i)^{\mathrm{T}}(\mathbf{y}_i - \mathbf{X}\tilde{\boldsymbol{\beta}}_i)],$$

which leads to

$$LLd = \log \tilde{P}(\mathbf{y}|H_d) = -n\log 2\pi\tilde{\sigma}_{H_d}^2 - n.$$

As a result, the likelihood ratio is given by

$$LR = \frac{\hat{P}(\mathbf{y}|H_a)}{\tilde{P}(\mathbf{y}|H_d)} = \left(\frac{\tilde{\sigma}_{H_d}^2}{\hat{\sigma}_{H_a}^2}\right)^n.$$

This test statistic can be written as

$$t_3 = (LR)^{1/n} - 1 = \frac{\tilde{\sigma}_{H_d}^2 - \hat{\sigma}_{H_a}^2}{\hat{\sigma}_{H_a}^2} = \frac{1}{\hat{\sigma}_{H_a}^2}[(\mathbf{y}_r - \mathbf{X}\tilde{\boldsymbol{\beta}}_r)^{\mathrm{T}}(\mathbf{y}_r - \mathbf{X}\tilde{\boldsymbol{\beta}}_r)$$

$$- (\mathbf{y}_r - \mathbf{X}\hat{\boldsymbol{\beta}}_r)^{\mathrm{T}}(\mathbf{y}_r - \mathbf{X}\hat{\boldsymbol{\beta}}_r) + (\mathbf{y}_i - \mathbf{X}\tilde{\boldsymbol{\beta}}_i)^{\mathrm{T}}(\mathbf{y}_i - \mathbf{X}\tilde{\boldsymbol{\beta}}_i)$$

$$- (\mathbf{y}_i - \mathbf{X}\hat{\boldsymbol{\beta}}_i)^{\mathrm{T}}(\mathbf{y}_i - \mathbf{X}\hat{\boldsymbol{\beta}}_i)]$$

After a few steps we can write

$$(\mathbf{y}_r - \mathbf{X}\tilde{\boldsymbol{\beta}}_r)^T(\mathbf{y}_r - \mathbf{X}\tilde{\boldsymbol{\beta}}_r) - (\mathbf{y}_r - \mathbf{X}\hat{\boldsymbol{\beta}}_r)^T(\mathbf{y}_r - \mathbf{X}\hat{\boldsymbol{\beta}}_r)$$

$$= \mathbf{v}^T\hat{\boldsymbol{\beta}}_r[\mathbf{v}^T(\mathbf{X}^T\mathbf{X})^{-1}\mathbf{v}]^{-1}\hat{\boldsymbol{\beta}}_r^T\mathbf{v},$$

$$(\mathbf{y}_i - \mathbf{X}\tilde{\boldsymbol{\beta}}_i)^T(\mathbf{y}_i - \mathbf{X}\tilde{\boldsymbol{\beta}}_i) - (\mathbf{y}_i - \mathbf{X}\hat{\boldsymbol{\beta}}_i)^T(\mathbf{y}_i - \mathbf{X}\hat{\boldsymbol{\beta}}_i)$$

$$= \mathbf{v}^T\hat{\boldsymbol{\beta}}_i[\mathbf{v}^T(\mathbf{X}^T\mathbf{X})^{-1}\mathbf{v}]^{-1}\hat{\boldsymbol{\beta}}_i^T\mathbf{v}.$$

Therefore the test statistic can be finally integrated as one expression as

$$t_3 = \frac{1}{\hat{\sigma}^2_{H_a}}\mathbf{v}^T\hat{\boldsymbol{\beta}}[\mathbf{v}^T(\mathbf{X}^T\mathbf{X})^{-1}\mathbf{v}]^{-1}\hat{\boldsymbol{\beta}}^T\mathbf{v}, \qquad [A5]$$

This is equivalent to Eq. [A4] and shows that the two methods possess the same test statistics.

REFERENCES

1. Hoogenraad FG, Reichenbach JR, Haacke EM, Lai S, Kuppusamy K, Sprenger M. In vivo measurement of changes in venous blood-oxygenation with high resolution functional MRI at 0.95 Tesla by measuring changes in susceptibility and velocity. Magn Reson Med 1998;39:97–107.
2. Menon RS. Postacquisition suppression of large-vessel BOLD signals in high-resolution fMRI. Magn Reson Med 2002;47:1–9.
3. Cho ZH, Ro YM, Chung SC, Chung JY. A direct susceptibility measurement in fMRI using SSFP interferometry (SSFPI) technique. In: Proceedings of the 3rd Annual Meeting of SMR, Nice, France, 1995. p 806.
4. Scheffler K, Seifritz E, Bilecen D, Venkatesan R, Hennig J, Deimling M, Haacke EM. Detection of BOLD changes by means of a frequencysensitive trueFISP technique: preliminary results. NMR Biomed 2001;14:490–496.
5. Miller KL, Hargreaves BA, Lee J, Ress D, deCharms RC, Pauly JM. Functional brain imaging using a blood oxygenation sensitive steady state. Magn Reson Med 2003;50:675–683.
6. Miller KL, Smith SM, Jezzard P, Pauly JM. High-resolution FMRI at 1.5T using balanced SSFP. Magn Reson Med 2006;55:161–170
7. Lai S, Glover GH. Detection of BOLD fMRI signals using complex data. In: Proceedings of the 5th Annual Meeting of ISMRM, Vancouver, Canada, 1997 (Abstract 1671).
8. Rowe DB, Logan BR. A complex way to compute fMRI activation. Neuroimage 2004;23:1078–1092.
9. Rowe DB. Modeling both the magnitude and phase of complex-valued fMRI data. Neuroimage 2005;25:1310–1324.
10. Sijbers J, den Dekker AJ. Generalized likelihood ratio tests for complex fMRI data: a simulation study. IEEE Trans Med Imaging 2005;24:604–611.
11. Rowe DB, Logan BR. Complex fMRI analysis with unrestricted phase is equivalent to a magnitude-only model. Neuroimage 2005;24:603–606.
12. Rowe DB. Parameter estimation in the magnitude-only and complex-valued fMRI data models. Neuroimage 2005;25:1124–1132.
13. Nan FY, Nowak RD. Generalized likelihood ratio detection for fMRI using complex data. IEEE Trans Med Imaging 1999;18:320–329.
14. Rowe DB, Nencka AS. Complex activation suppresses venous BOLD in GE-EPI fMRI data. In: Proceedings of the 14th Annual Meeting of ISMRM, Seattle, WA, USA, 2006 (Abstract 2834).
15. Nencka AS, Rowe DB. Theoretical results demonstrate fundamental differences in venous BOLD reducing activation methods. In: Proceedings of the 14th Annual Meeting of ISMRM, Seattle, WA, USA, 2006 (Abstract 3269).
16. Srivastava MS. Methods of multivariate statistics. New York: John Wiley & Sons; 2002. p 89–151.
17. Friston KJ, Holmes AP, Poline JB, Grasby PJ, Williams SC, Frackowiak RS, Turner R. Analysis of fMRI time-series revisited. Neuroimage 1995;2:45–53.
18. Chu SC, Xu Y, Balschi JA, Springer Jr CS. Bulk magnetic susceptibility shifts in NMR studies of compartmentalized samples: use of paramagnetic reagents. Magn Reson Med 1990;13:239–262.
19. Boxerman JL, Hamberg LM, Rosen BR, Weisskoff RM. MR contrast due to intravascular magnetic susceptibility perturbations. Magn Reson Med 1995;34:555–566.
20. Spees WM, Yablonskiy DA, Oswood MC, Ackerman JJ. Water proton MR properties of human blood at 1.5 Tesla: magnetic susceptibility, T, T, T*, and non-Lorentzian signal behavior. Magn Reson Med 2001;45:533–542.
21. Reichenbach JR, Venkatesan R, Schillinger DJ, Kido DK, Haacke EM. Small vessels in the human brain: MR venography with deoxyhemoglobin as an intrinsic contrast agent. Radiology 1997;204:272–277.
22. Frackowiak RSJ, Friston KJ, Frith CD, Dolan RJ, Mazziotta JC. Human brain function. London: Academic Press; 1997.
23. Smith SM, Jenkinson M, Woolrich MW, Beckmann CF, Behrens TE, Johansen-Berg H, Bannister PR, De Luca M, Drobnjak I, Flitney DE, Niazy RK, Saunders J, Vickers J, Zhang Y, De Stefano N, Brady JM, Matthews PM. Advances in functional and structural MR image analysis and implementation as FSL [Review]. Neuroimage 2004;23(Suppl 1):S208–S219.
24. Yablonskiy DA, Haacke EM. Theory of NMR signal behavior in magnetically inhomogeneous tissues: the static dephasing regime. Magn Reson Med 1994;32:749–763.
25. Silvennoinen MJ, Clingman CS, Golay X, Kauppinen RA, van Zijl PC. Comparison of the dependence of blood R2 and R2* on oxygen saturation at 1.5 and 4.7 Tesla. Magn Reson Med 2003;49:47–60.
26. Song AW, Wong EC, Tan SG, Hyde JS. Diffusion weighted fMRI at 1.5 T. Magn Reson Med 1996;35:155–158.
27. Lee J, Santos JM, Conolly SM, Miller KL, Hargreaves BA, Pauly JM. Respiration-induced B0 field fluctuation compensation in balanced SSFP: real-time approach for transition-band SSFP fMRI. Magn Reson Med 2006;55:1197–1201.
28. Boxerman JL, Bandettini PA, Kwong KK, Baker JR, Davis TL, Rosen BR, Weisskoff RM. The intravascular contribution to fMRI signal change: Monte Carlo modeling and diffusion-weighted studies in vivo. Magn Reson Med 1995;34:4–10.
29. Lee SP, Silva AC, Ugurbil K, Kim SG. Diffusion-weighted spin-echo fMRI at 9.4 T: microvascular/tissue contribution to BOLD signal changes. Magn Reson Med 1999;42:919–928.
30. Hulvershorn J, Bloy L, Gualtieri EE, Leigh JS, Elliott MA. Spatial sensitivity and temporal response of spin echo and gradient echo bold contrast at 3 T using peak hemodynamic activation time. Neuroimage 2005;24:216–223.
31. Barth M, Norris DG. High resolution 3D fMRI of human visual cortex with elimination of large venous vessels. In: Proceedings of the 14th Annual Meeting of ISMRM, Seattle, WA, USA, 2006 (Abstract 893).
32. Oja JM, Gillen J, Kauppinen RA, Kraut M, van Zijl PC. Venous blood effects in spin-echo fMRI of human brain. Magn Reson Med 1999;42:617–626.
33. Shahram M, Milanfar P. Statistical and information—theoretic analysis of resolution in imaging. IEEE Trans Info Theory 2006;52:3411–3437.
34. Kay SM. Fundamentals of statistical signal processing: estimation theory. Saddle River, New Jersey: Prentice-Hall; 1993. p 251–252.